

Supporting Information

Dissecting reconstructed anions in sulfides as a role in urea oxidation to maximize assisted hydrogen production

Weiwei Bao^{a,1}, Mameng Yang^{a,1}, Taotao Ai^{a,*}, Jie Han^{a,*}, Zhifeng Deng^a, Xiangyu Zou^a, Peng Jiang^a, Junjun Zhang^b

^aNational and Local Joint Engineering Laboratory for Slag Comprehensive Utilization and Environmental Technology, School of Materials Science and Engineering, Shaanxi University of Technology, Hanzhong 723000, Shaanxi, PR China.

^bState Key Laboratory of High-efficiency Utilization of Coal and Green Chemical Engineering, College of Chemistry & Chemical Engineering, Ningxia University, Yinchuan 750021, Ningxia, PR China.

¹ These authors contributed equally to this work

***Corresponding author at:** School of Materials Science and Engineering, Shaanxi University of Technology, No. 1 Dongyihuan, Hantai District, Hanzhong 723000, PR China, 18691612234 (T. Ai)

E-mail addresses: aitaotao0116@126.com (T. Ai); 805160700@qq.com (J. Han).

List of Contents

Experimental Section:

1. Treatment of Ni foam
2. Chemicals and Reagents
3. Electrochemical measurements.
4. In situ Raman spectroscopy.
5. Theoretical calculations.

Supporting Figures and Tables:

Figure S1. SEM images of NF (a, b) at different magnifications.

Figure S2. SEM images of Mo₃₁-Ni₃S₂ (a, b), Mo₆₅-Ni₃S₂ (b, c) and Mo₈₂-Ni₃S₂ (e, f) at different magnifications.

Figure S3. XRD pattern of Mo_x-Ni₃S₂ samples with different doping ratios.

Figure S4. Comparison of CV curves for (a) Ni₃S₂, (b) Mo₃₁-Ni₃S₂, (c) Mo₄₈-Ni₃S₂, (d) Mo₆₅-Ni₃S₂, and (e) Mo₈₂-Ni₃S₂ in 1 M KOH+0.5 M urea at different scan rates from 20 mV s⁻¹ to 100 mV s⁻¹.

Figure S5. Nyquist plots for different doping ratios of Mo_x-Ni₃S₂ in 0.5 M urea solution.

Figure S6. Comparison of UOR performance of the present work with other transition metal-based catalysts at a current density of 100 mA cm⁻².

Figure S7. LSV plot of Ni(OH)₂ in KOH + 0.5 M Urea.

Figure S8. EIS plots for different concentrations of MoO₄²⁻ added to Ni(OH)₂.

Figure S9. Comparison of CV curves for Ni(OH)₂ in (a) KOH, (b) KOH+0.01 M MoO₄²⁻, (c) KOH+0.05 M MoO₄²⁻, (d) KOH+0.1 M MoO₄²⁻, and (e) KOH+0.15 M MoO₄²⁻ at different scan rates from 20 mV s⁻¹ to 100 mV s⁻¹; (f) C_{dl} plots.

Figure S10. Stability of Ni(OH)₂ in the presence of 0.1 M MoO₄²⁻ at the potential of 0.86 V.

Figure S11. EIS plots for different concentrations of SO₄²⁻ added to Ni(OH)₂.

Figure S12. Comparison of CV curves for Ni(OH)₂ in (a) KOH, (b) KOH+0.01 M SO₄²⁻, (c) KOH+0.05 M SO₄²⁻, (d) KOH+0.1 M SO₄²⁻, and (e) KOH+0.15 M SO₄²⁻ at different scan rates from 20 mV s⁻¹ to 100 mV s⁻¹; (f) C_{dl} plots.

Figure S13. Stability of Ni(OH)₂ in the presence of 0.1 M SO₄²⁻ at the potential of 0.77 V.

Figure S14. EIS plots van Ni(OH)₂ in KOH and KOH+0.1 M MoO₄²⁻+0.1 M SO₄²⁻.

Figure S15. Comparison of CV curves for Ni(OH)₂ in (a) KOH, (b) KOH+0.01 M MoO₄²⁻+0.1 M SO₄²⁻; (c) C_{dl} plots.

Figure S16. Stability of Ni(OH)₂ in the presence of 0.1 M MoO₄²⁻+0.1 M SO₄²⁻ at the potential of 0.85 V.

Figure S17. Faraday efficiency and gas collection of Ni(OH)₂ with the addition of 0.1 M MoO₄²⁻+0.1 M SO₄²⁻ at a potential of 0.85 V.

Figure S18. (a) LSV plot, (b) overpotential plot, (c) Tafel plot and (d) EIS plot van Ni(OH)₂ in KOH, KOH+0.1 M MoO₄²⁻, KOH+0.1 M SO₄²⁻ and KOH+0.1 M MoO₄²⁻+0.1 M SO₄²⁻.

Figure S19. NiOOH optimization structure model under different UOR steps.

Figure S20. NiOOH+MoO₄²⁻+SO₄²⁻ optimization structure model under different UOR steps.

Figure S21. Comparison of CV curves for (a) Ni₃S₂, (b) Mo₃₁-Ni₃S₂, (c) Mo₄₈-Ni₃S₂, (d) Mo₆₅-Ni₃S₂, and (e) Mo₈₂-Ni₃S₂ in 1 M KOH at different scan rates from 20 mV s⁻¹ to 100 mV s⁻¹.

Figure S22. Comparison of HER performance of the present work with other transition metal-based catalysts at a current density of 100 mA cm⁻².

Figure S23. Nyquist plots for different doping ratios of Mo_x-Ni₃S₂ in 1 M KOH solution.

Figure S24. Chronopotentiometry measurements at 100 mA cm⁻² for Mo₄₈-Ni₃S₂ (inset: SEM images of Mo₄₈-Ni₃S₂ after HER test).

Figure S25. (a) in-situ Raman spectra of Mo₄₈-Ni₃S₂ in the HER process; (b) In situ Raman contour map.

Table S1. Comparison of UOR performances for Mo₄₈-Ni₃S₂ with various reported electrocatalysts in the alkaline media with urea.

Table S2. Measured pH of 1.0 M KOH with the addition of different concentrations of MoO₄²⁻.

Table S3. Measured pH of 1.0 M KOH with the addition of different concentrations of SO₄²⁻.

Table S4. Comparison of HER performances for Mo₄₈-Ni₃S₂ with various reported electrocatalysts in the alkaline media with urea.

Table S5. The potential required for a noble metal-based electrocatalyst in 0.5 M urea solution at 10 mA cm⁻² has recently been reported.

Experimental Procedures

1. Treatment of Ni foam

The nickel foam (NF, 1×4 cm) was immersed in 2 M hydrochloric acid, ethanol and distilled water, respectively, for ultrasonic treatment over 12 min. which was dried at 60 °C for 8 h. After cooling to room temperature, it was obtained.

2. Chemicals and Reagents

Thioacetamide (C_2H_5NS) comes from Shanghai Macklin Biochemical Technology Co., Ltd. Sodium molybdate dehydrate ($Na_2MoO_4 \cdot 2H_2O$) is purchased from Sinopharm Chemical Reagent Co., Ltd. Nickel foam (NF) is used as substrate. All these chemicals are used without further purification.

3. Electrochemical measurements.

All the electrochemical measurements were conducted in a standard three-electrode setup on a CHI 660E electrochemical workstation (Chenhua Instruments, Shanghai, China). The fabricated self-supported electrodes ($1 \times 4 \times 0.1 \text{ cm}^2$) were directly employed as working electrodes, while a graphite rod and an Hg/HgO (filled in 1 M KOH) electrode as the counter electrode and the reference electrode, respectively. Before Multiple cyclic voltammetry (CV) scans were firstly performed at a scan rate of 5 mV s^{-1} until reached a stable state of electrodes. Then, linear sweep voltammetry (LSV) was conducted with a scan rate of 5 mV s^{-1} in 1 M KOH solution. The electrochemical impedance spectroscopy (EIS) measurements were conducted over a frequency range of 100 kHz to 0.01 Hz with an amplitude of 10 mV. The long-term stability was measured by chronocurrent method. All the polarization curves were corrected using 85% iR compensation. Potentials were referenced to the reversible hydrogen electrode (RHE): $E \text{ vs. RHE} = E \text{ vs. Hg/HgO} + 0.098 + 0.059 \text{ pH}$. The overpotential (η) was calculated according to the following equation: $\eta = E \text{ vs. RHE} - 1.23 \text{ V}$. In order to obtain the effective electrochemical active surface area (ECSA) of the electrocatalyst, a series of cyclic voltammetry (CV) measurements were performed at different scanning rates. Geometric double layer capacitance (C_{dl}) is calculated by plotting the difference between current density (J) and scan rate to build a linear trend.

4. In situ Raman spectroscopy.

The in-situ device was placed on a Renishaw Raman microscope, the potential was controlled by an electrochemical workstation, and the Raman spectra were recorded by 532 nm laser excitation. In situ device electrolytic cell is made of polytetrafluoroethylene, through the large pool, small pool, electrolyte and pump to form a closed loop, the top with a round quartz glass as a protective cover to protect the objective lens, the working electrode is facing the quartz glass, so that the laser is vertically incident, before the test should increase the pump rate, the circulation of bubbles clean, avoid blocking the light path, after stabilizing, reduce the speed for testing. The Hg/HgO electrode with 1.0 M KOH internal reference electrolyte was used as the reference electrode.

5. Theoretical calculations.

All the calculations were performed with the Vienna Ab initio Simulation Package (VASP) based on the density-functional theory (DFT). We use DFT to help understand the reaction mechanism. The generalized gradient approximation (GGA) with Perdew-Burke-Ernzerhof (PBE) functional is used, and the long-range van der Waals interaction is considered using the DFT-D3 method, the cut off energy is 500 eV, and the K point is $3 \times 2 \times 1$. A 4×4 supercell model was constructed using Ni(OH)₂ (112) surfaces. A 15 Å vacuum is used along the z direction to avoid interaction between periodic images. The convergence criteria for electrons and ions are 10^{-7} eV energies and 0.05 eV Å⁻¹ forces to ensure adequate accuracy.

Supporting Figures and Tables

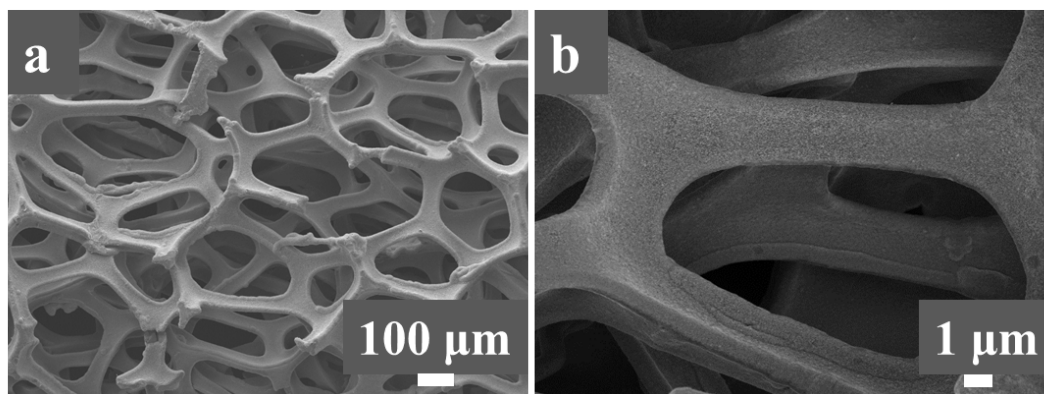


Figure S1. SEM images of NF (a, b) at different magnifications.

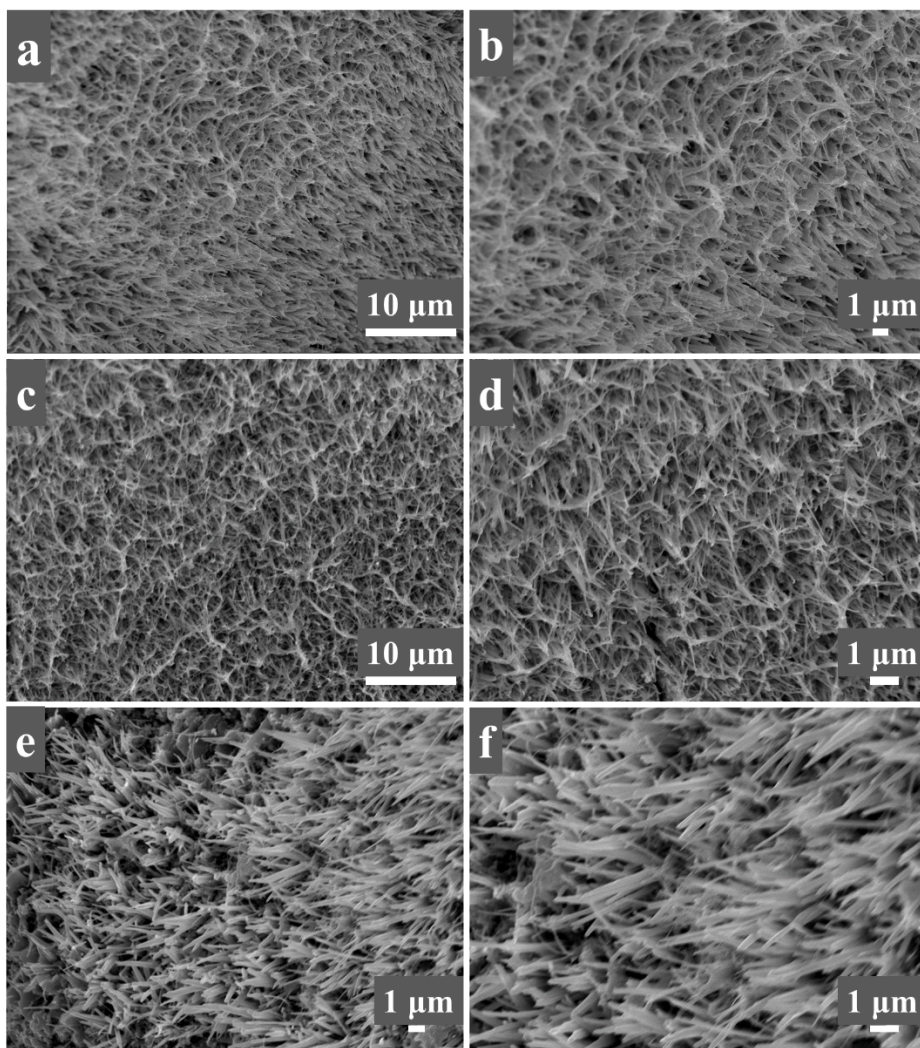


Figure S2. SEM images of Mo₃₁-Ni₃S₂ (a, b), Mo₆₅-Ni₃S₂ (b, c) and Mo₈₂-Ni₃S₂ (e, f) at different magnifications.

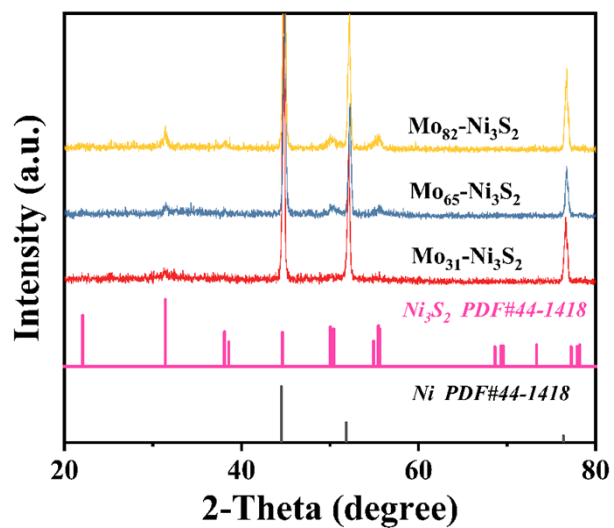


Figure S3. XRD pattern of $\text{Mo}_x\text{-Ni}_3\text{S}_2$ samples with different doping ratios.

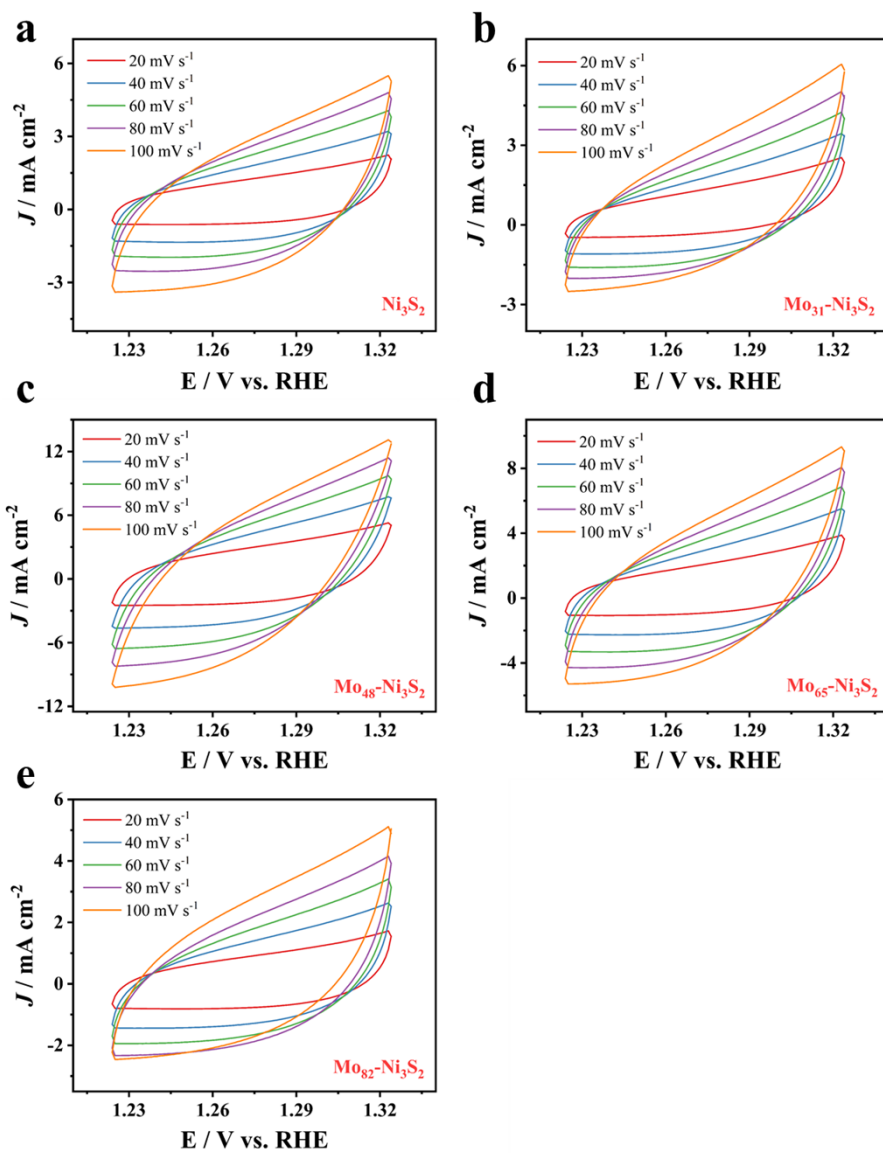


Figure S4. Comparison of CV curves for (a) Ni_3S_2 , (b) $\text{Mo}_{31}\text{-Ni}_3\text{S}_2$, (c) $\text{Mo}_{48}\text{-Ni}_3\text{S}_2$, (d) $\text{Mo}_{65}\text{-Ni}_3\text{S}_2$, and (e) $\text{Mo}_{82}\text{-Ni}_3\text{S}_2$ in 1 M KOH+0.5 M urea at different scan rates from 20 mV s^{-1} to 100 mV s^{-1} .

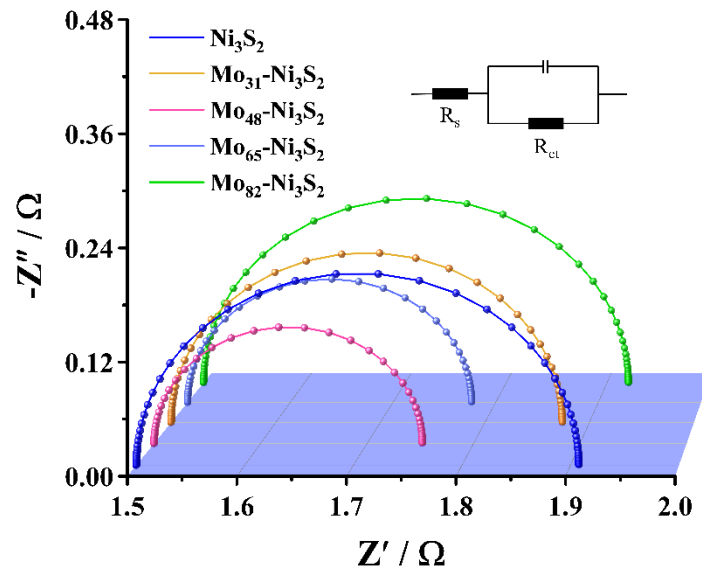


Figure S5. Nyquist plots for different doping ratios of $\text{Mo}_x\text{-Ni}_3\text{S}_2$ in 0.5 M urea solution.

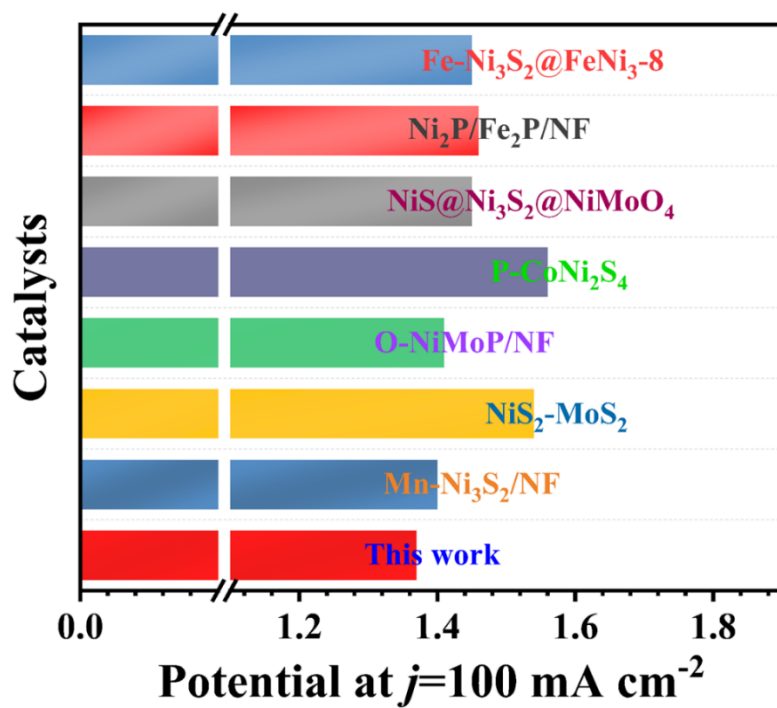


Figure S6. Comparison of UOR performance of the present work with other transition metal-based catalysts at a current density of 100 mA cm^{-2} .

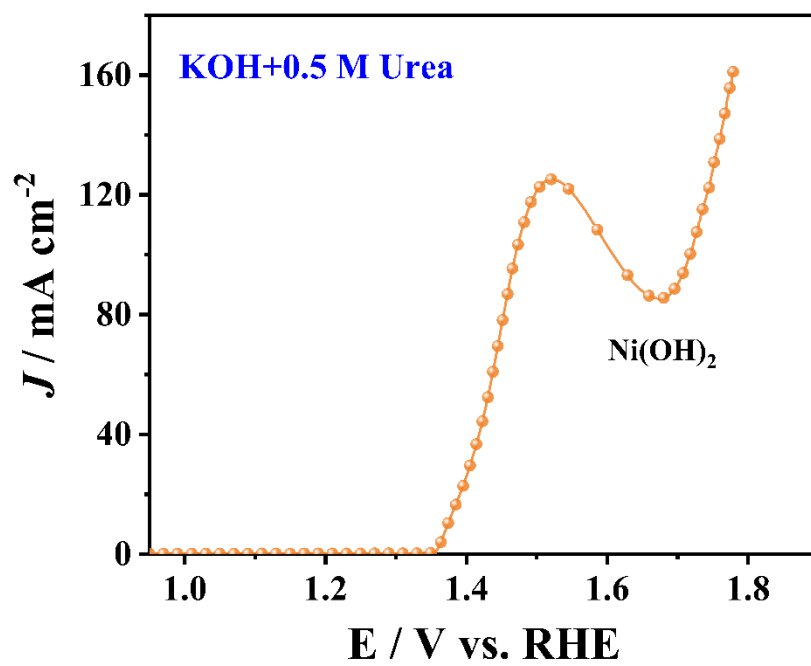


Figure S7. LSV plot of Ni(OH)_2 in $\text{KOH} + 0.5 \text{ M Urea}$.

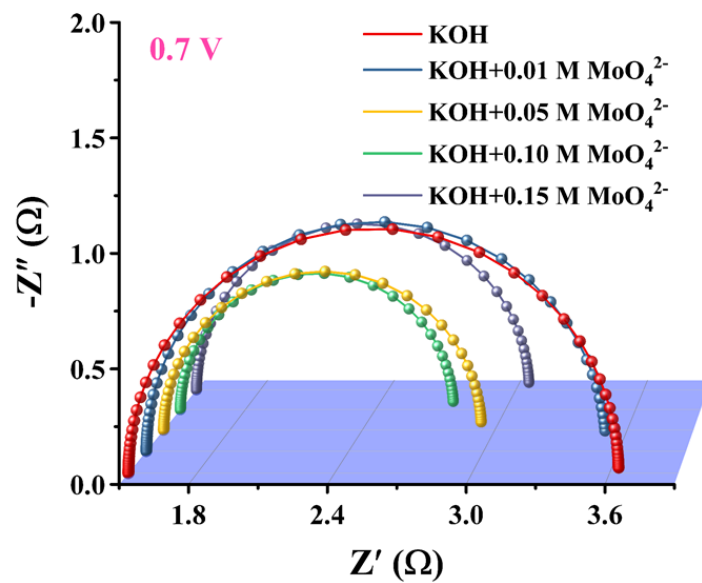


Figure S8. EIS plots for different concentrations of MoO_4^{2-} added to Ni(OH)_2 .

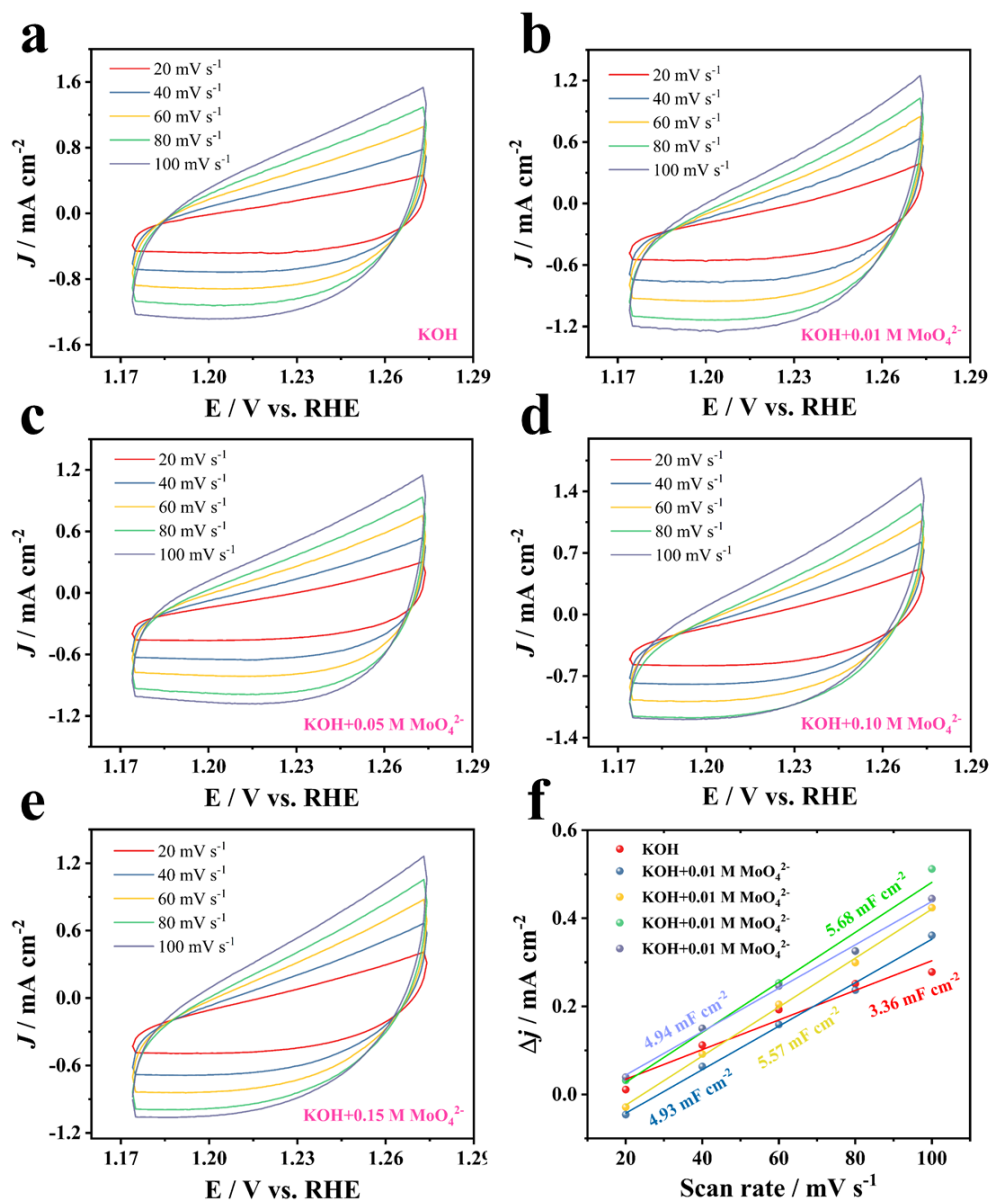


Figure S9. Comparison of CV curves for Ni(OH)_2 in (a) KOH, (b) KOH+0.01 M MoO_4^{2-} , (c) KOH+0.05 M MoO_4^{2-} , (d) KOH+0.1 M MoO_4^{2-} , and (e) KOH+0.15 M MoO_4^{2-} at different scan rates from 20 mV s^{-1} to 100 mV s^{-1} ; (f) C_{dl} plots.

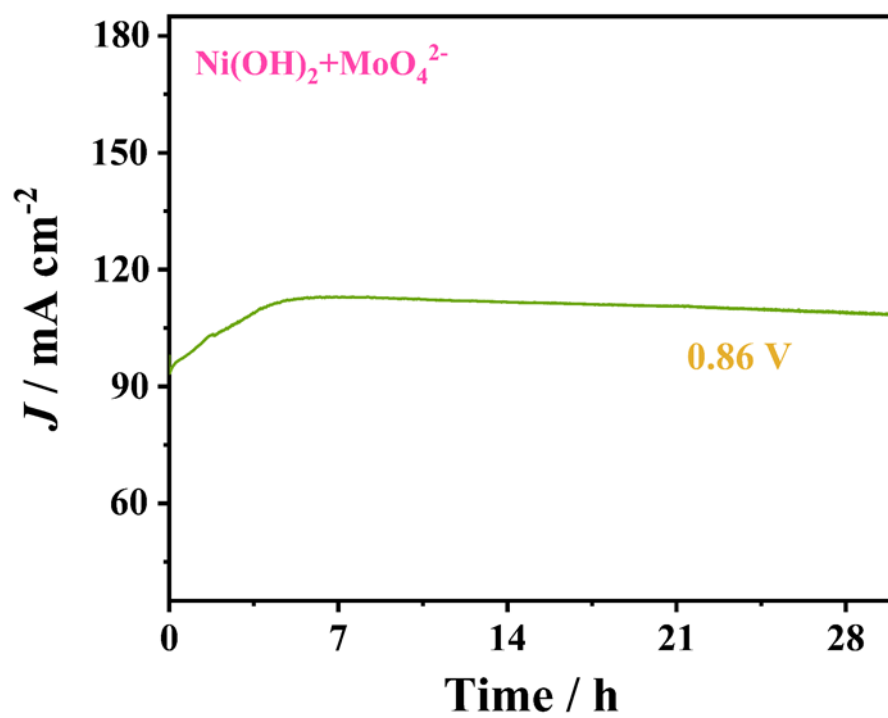


Figure S10. Stability of Ni(OH)_2 in the presence of 0.1 M MoO_4^{2-} at the potential of 0.86 V .

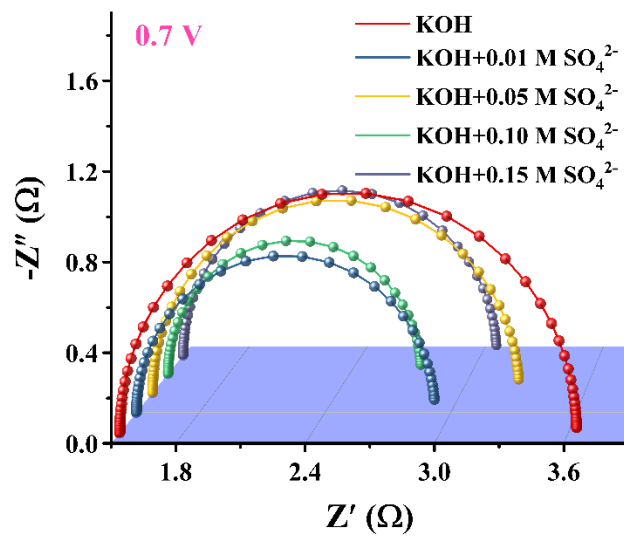


Figure S11. EIS plots for different concentrations of SO₄²⁻ added to Ni(OH)₂.

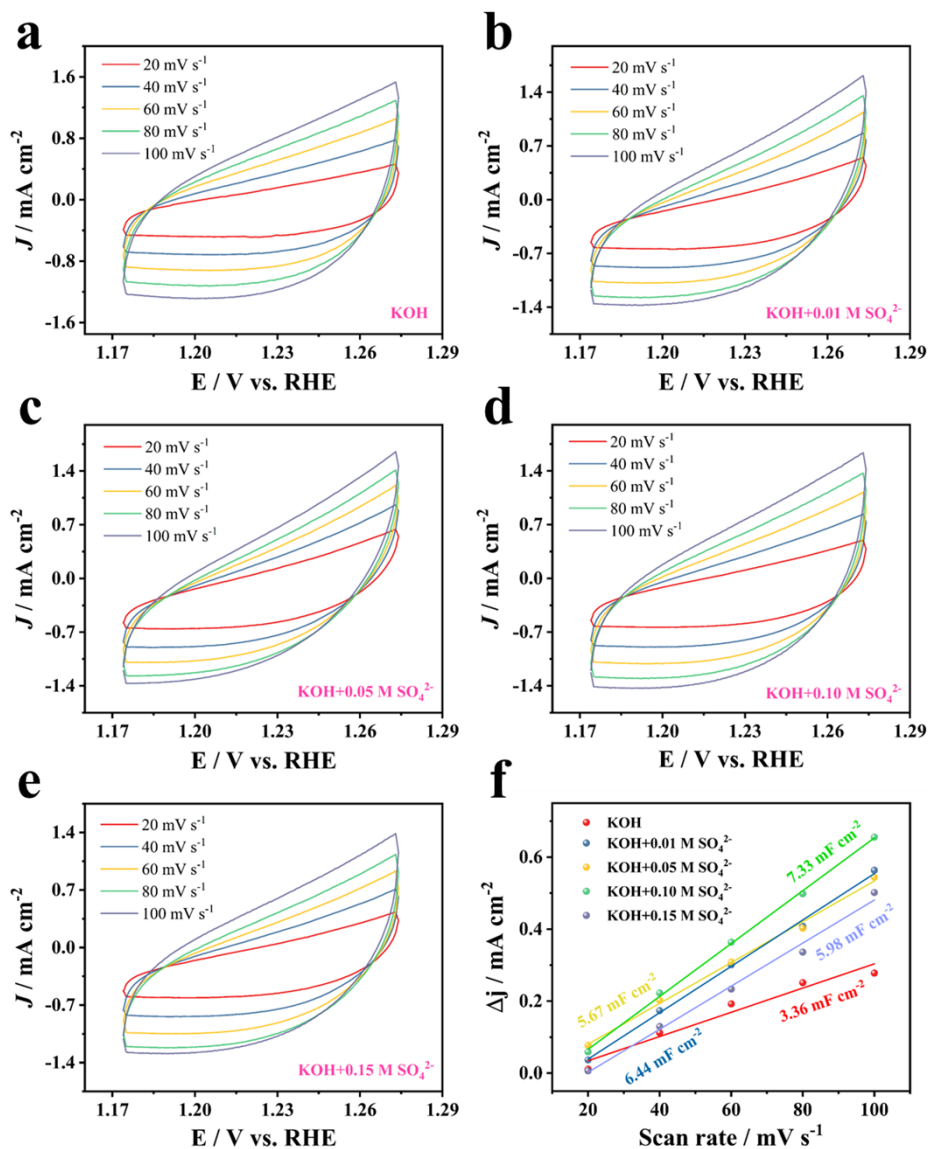


Figure S12. Comparison of CV curves for Ni(OH)_2 in (a) KOH , (b) $\text{KOH} + 0.01 \text{ M SO}_4^{2-}$, (c) $\text{KOH} + 0.05 \text{ M SO}_4^{2-}$, (d) $\text{KOH} + 0.1 \text{ M SO}_4^{2-}$, and (e) $\text{KOH} + 0.15 \text{ M SO}_4^{2-}$ at different scan rates from 20 mV s^{-1} to 100 mV s^{-1} ; (f) C_{dl} plots.

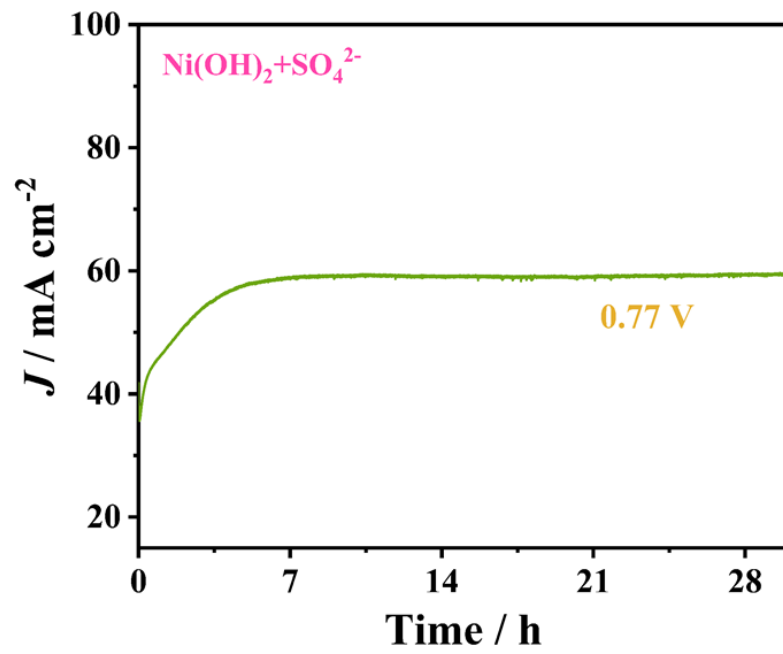


Figure S13. Stability of Ni(OH)_2 in the presence of 0.1 M SO_4^{2-} at the potential of 0.77 V .

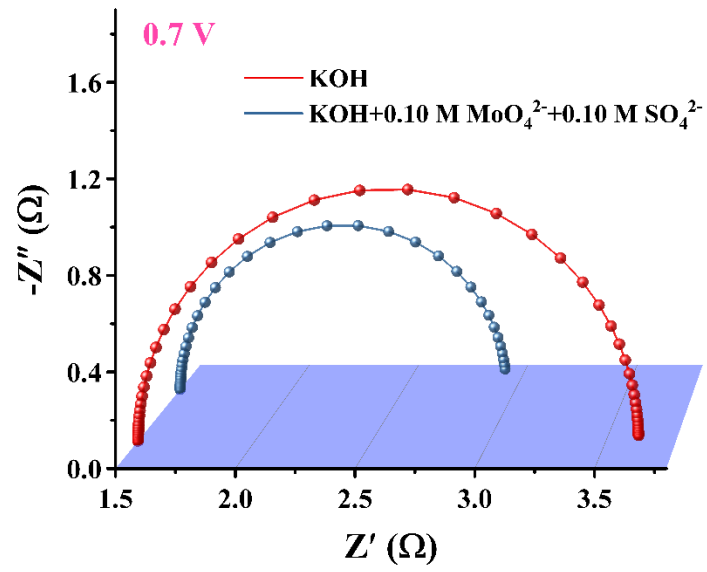


Figure S14. EIS plots van Ni(OH)₂ in KOH and KOH+0.1 M MoO₄²⁻+0.1 M SO₄²⁻.

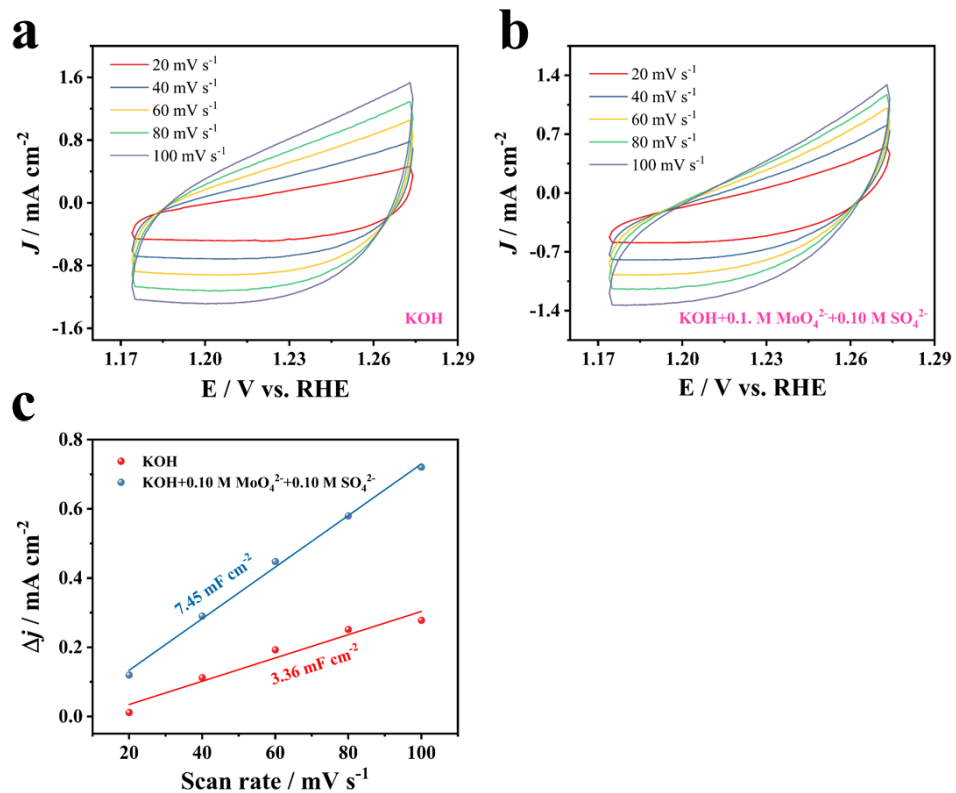


Figure S15. Comparison of CV curves for Ni(OH)₂ in (a) KOH, (b) KOH+0.01 M MoO_4^{2-} +0.1 M SO_4^{2-} ; (c) C_{dl} plots.

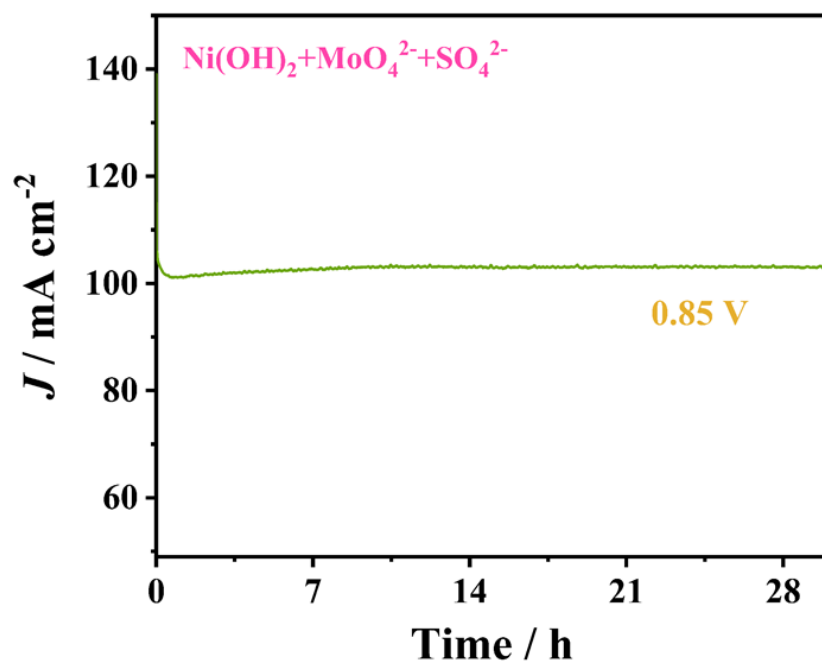


Figure S16. Stability of Ni(OH)_2 in the presence of $0.1 \text{ M MoO}_4^{2-} + 0.1 \text{ M SO}_4^{2-}$ at the potential of 0.85 V .

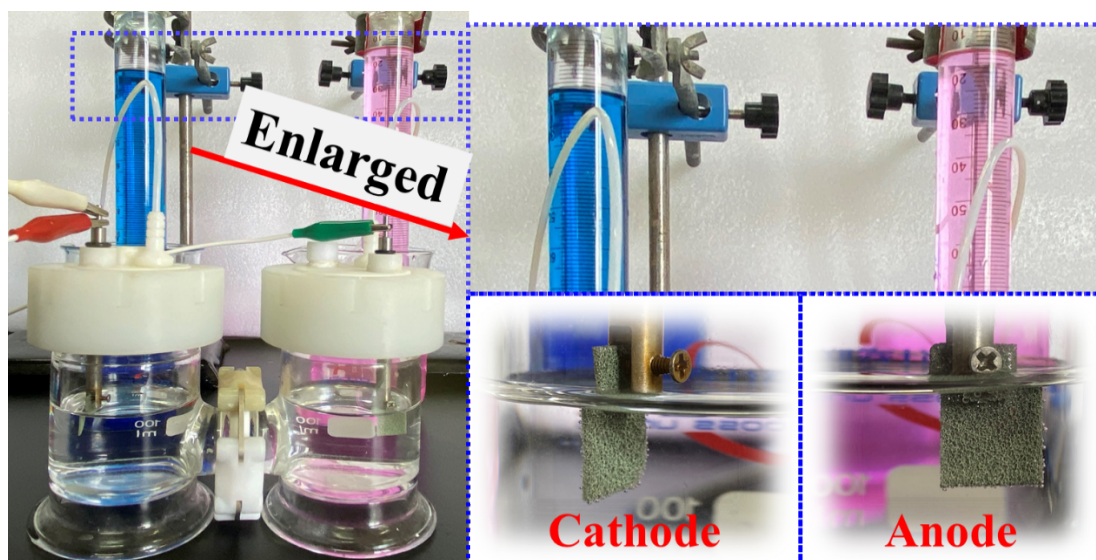


Figure S17. Faraday efficiency and gas collection of $\text{Ni}(\text{OH})_2$ with the addition of $0.1 \text{ M MoO}_4^{2-} + 0.1 \text{ M SO}_4^{2-}$ at a potential of 0.85 V .

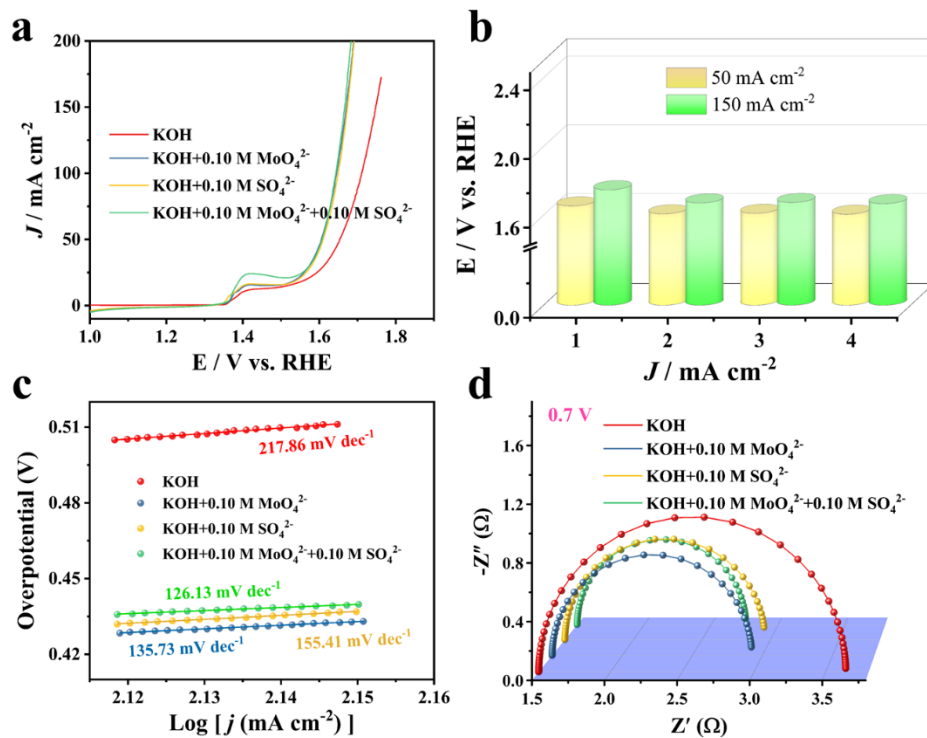


Figure S18. (a) LSV plot, (b) overpotential plot, (c) Tafel plot and (d) EIS plot van Ni(OH)_2 in KOH, KOH+0.1 M MoO_4^{2-} , KOH+0.1 M SO_4^{2-} and KOH+0.1 M MoO_4^{2-} +0.1 M SO_4^{2-} .

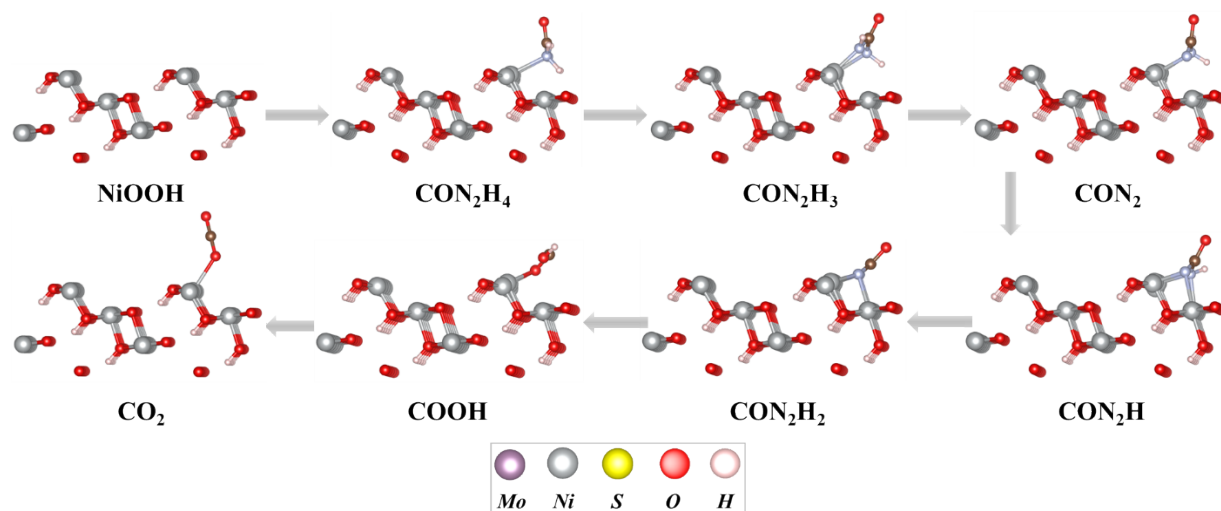


Figure S19. NiOOH optimization structure model under different UOR steps.

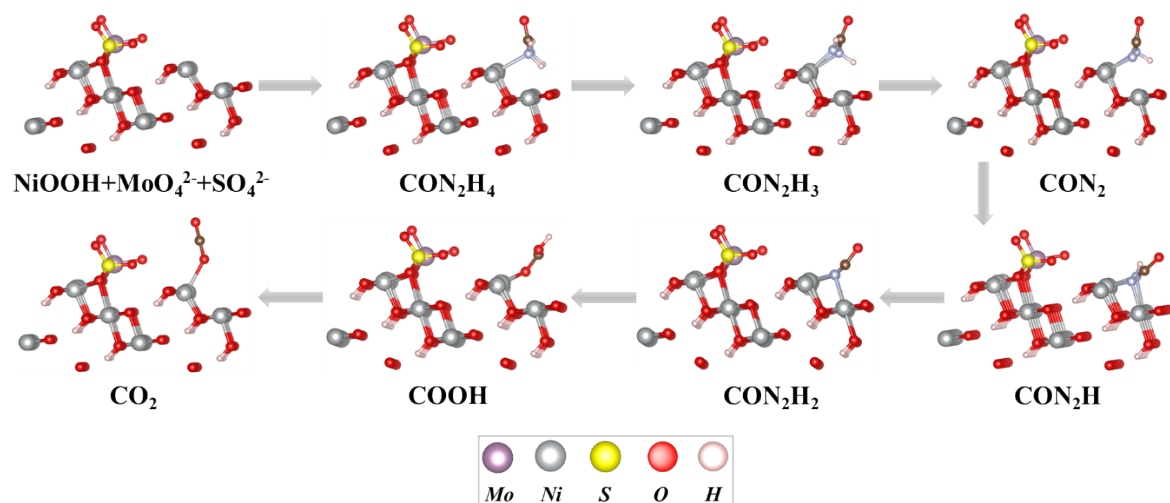


Figure S20. $\text{NiOOH} + \text{MoO}_4^{2-} + \text{SO}_4^{2-}$ optimization structure model under different UOR steps.

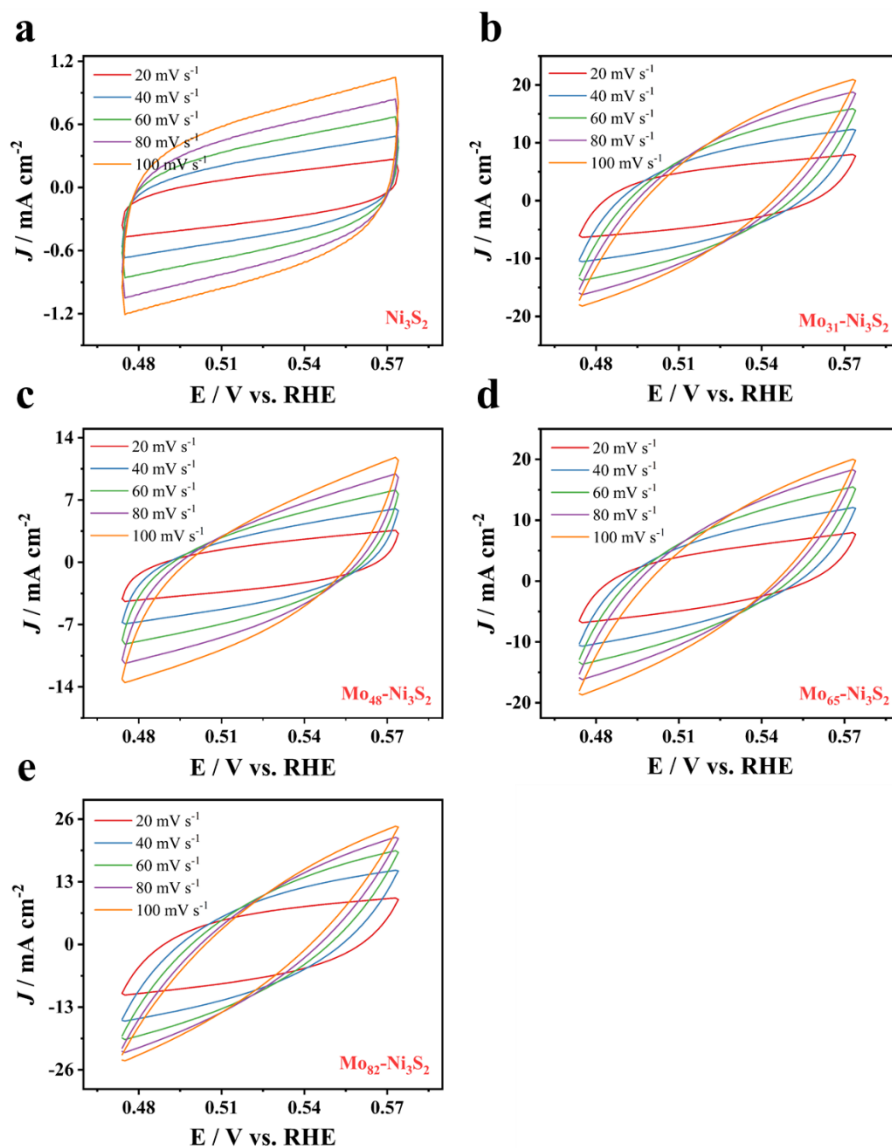


Figure S21. Comparison of CV curves for (a) Ni_3S_2 , (b) $\text{Mo}_{31}\text{-Ni}_3\text{S}_2$, (c) $\text{Mo}_{48}\text{-Ni}_3\text{S}_2$, (d) $\text{Mo}_{65}\text{-Ni}_3\text{S}_2$, and (e) $\text{Mo}_{82}\text{-Ni}_3\text{S}_2$ in 1 M KOH at different scan rates from 20 mV s^{-1} to 100 mV s^{-1} .

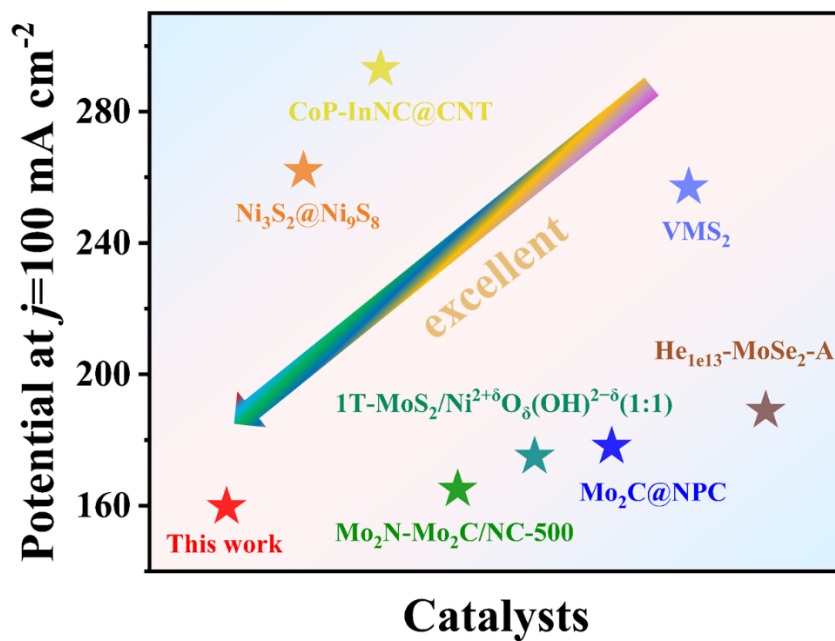


Figure S22. Comparison of HER performance of the present work with other transition metal-based catalysts at a current density of 100 mA cm^{-2} .

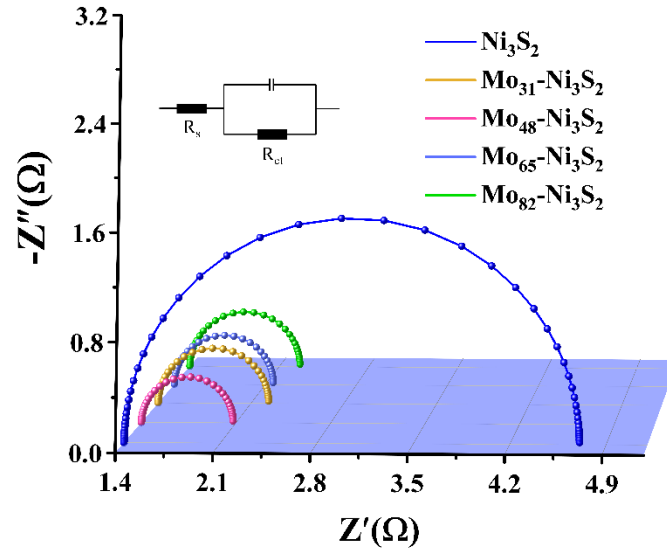


Figure S23. Nyquist plots for different doping ratios of Mo_x-Ni₃S₂ in 1 M KOH solution.

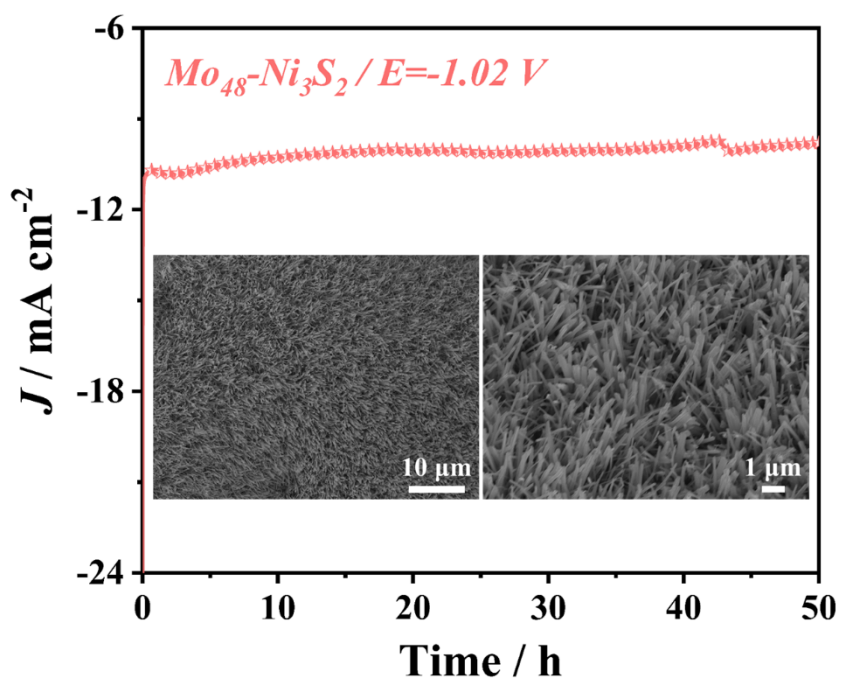


Figure S24. Chronoamperometry measurements at 100 mA cm^{-2} for $\text{Mo}_{48}\text{-Ni}_3\text{S}_2$ (inset: SEM images of $\text{Mo}_{48}\text{-Ni}_3\text{S}_2$ after HER test).

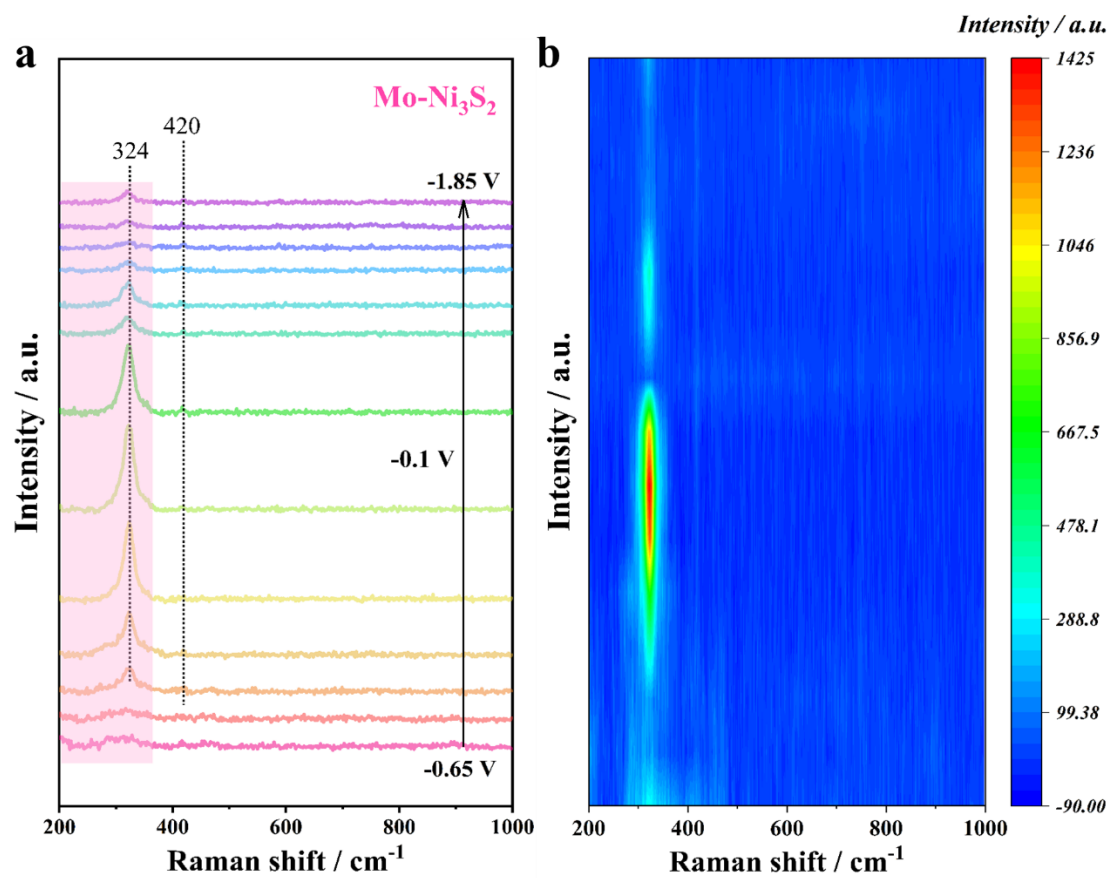


Figure S25. (a) in-situ Raman spectra of Mo₄₈-Ni₃S₂ in the HER process; (b) In situ Raman contour map.

Table S1. Comparison of UOR performances for Mo₄₈-Ni₃S₂ with various reported electrocatalysts in the alkaline media with urea.

electrocatalysts	electrolyte	Potential at 100 mA cm ⁻² (V)	Ref.
Fe-Ni ₃ S ₂ @FeNi ₃ -8	1.0 M KOH+ 0.33 M Urea	1.45	1
Ni ₂ P/Fe ₂ P/NF	1.0 M KOH+ 0.5 M Urea	1.46	2
NiS@Ni ₃ S ₂ @NiMoO ₄	1.0 M KOH+ 0.5 M Urea	1.45	3
P-CoNi ₂ S ₄	1.0 M KOH+ 0.5 M Urea	1.56	4
O-NiMoP/NF	1.0 M KOH+ 0.5 M Urea	1.41	5
NiS ₂ -MoS ₂	1.0 M KOH+ 0.33 M Urea	1.54	6
Mn-Ni ₃ S ₂ /NF	1.0 M KOH+ 0.5 M Urea	1.4	7
Mo ₄₈ -Ni ₃ S ₂	1.0 M KOH+ 0.5 M Urea	1.37	This work

Table S2. Measured pH of 1.0 M KOH with the addition of different concentrations of MoO_4^{2-} .

	KOH	+0.01	+0.05	+0.10	+0.15
		MoO_4^{2-}	MoO_4^{2-}	MoO_4^{2-}	MoO_4^{2-}
1st	13.59	13.58	13.56	13.56	13.57
2nd	13.60	13.57	13.55	13.58	13.58
3rd	13.58	13.59	13.58	13.59	13.59
Average	13.59	13.58	13.56333	13.57667	13.58

Table S3. Measured pH of 1.0 M KOH with the addition of different concentrations of SO_4^{2-} .

	KOH	+0.01 SO_4^{2-}	+0.05 SO_4^{2-}	+0.10 SO_4^{2-}	+0.15 SO_4^{2-}
1st	13.56	13.54	13.56	13.57	13.53
2nd	13.55	13.57	13.58	13.54	13.54
3rd	13.58	13.58	13.54	13.56	13.55
Average	13.56333	13.56333	13.55667	13.55667	13.54

Table S4. Comparison of HER performances for Mo₄₈-Ni₃S₂ with various reported electrocatalysts in the alkaline media with urea.

electrocatalysts	electrolyte	Potential at 100 mA cm ⁻² (mV)	Ref.
Ni ₃ S ₂ @Ni ₉ S ₈	1.0 M KOH	262	8
CoP-InNC@CNT	1.0 M KOH	293	9
Mo ₂ N-Mo ₂ C/NC-500	1.0 M KOH	165	10
1T-MoS ₂ /Ni ^{2+δ} O ₈ (OH) ^{2-δ} (1:1)	1.0 M KOH	175	11
Mo ₂ C@NPC	1.0 M KOH	178	12
VMS ₂	1.0 M KOH	257	13
He _{1e13} -MoSe ₂ -A	1.0 M KOH	198	14
Mo ₄₈ -Ni ₃ S ₂	1.0 M KOH	159.7	This work

Table S5. The potential required for a noble metal-based electrocatalyst in 0.5 M urea solution at 10 mA cm⁻² has recently been reported.

electrocatalysts	electrolyte	Potential at 10 mA cm ⁻² (mV)	Ref.
Ni(OH)S/NF	0.5 M Urea	1.36	15
P-CoNi ₂ S ₄	0.5 M Urea	1.4	4
NiS@Ni ₃ S ₂ /NiMoO ₄	0.5 M Urea	1.41	3
Ni-Mo nanotube	0.5 M Urea	1.43	16
Ni-S-Se/NF	0.5 M Urea	1.47	17
Ni ₂ P/Fe ₂ P/NF	0.5 M Urea	1.48	2
Mo ₄₈ -Ni ₃ S ₂	0.5 M Urea	1.34	This work

Reference:

- [1] W. Zhang, Q. Jia, H. Liang, L. Cui, D. Wei, J. Liu, Iron doped Ni₃S₂ nanorods directly grown on FeNi₃ foam as an efficient bifunctional catalyst for overall water splitting, *Chem. Eng. J.*, 2020, **395**, 125315.
- [2] L. Yan, Y. Sun, E. Hu, J. Ning, Y. Zhong, Z. Zhang, Y. Hu, Facile in-situ growth of Ni₂P/Fe₂P nanohybrids on Ni foam for highly efficient urea electrolysis, *J. Colloid Interface Sci.*, 2019, **541**, 279-286.
- [3] L. Sha, T. Liu, K. Ye, K. Zhu, J. Yan, J. Yin, G. Wang, D. Cao, A heterogeneous interface on NiS@ Ni₃S₂/NiMoO₄ heterostructures for efficient urea electrolysis, *J. Mater. Chem. A*, 2020, **8**, 18055-18063.
- [4] X. F. Lu, S. L. Zhang, W. L. Sim, S. Gao and X. W. D. Lou, Phosphorized CoNi₂S₄ Yolk-Shell Spheres for Highly Efficient Hydrogen Production via Water and Urea Electrolysis, *Angew. Chem. Int. Ed.*, 2021, **60**, 22885-22891.
- [5] H. Jiang, M. Sun, S. Wu, B. Huang, C. S. Lee, W. Zhang, Oxygen-Incorporated NiMoP Nanotube Arrays as Efficient Bifunctional Electrocatalysts For Urea-Assisted Energy-Saving Hydrogen Production in Alkaline Electrolyte, *Adv. Funct. Mater.*, 2021, **31**, 2104951.
- [6] S. Wang, L. Zhao, J. Li, X. Tian, X. Wu, L. Feng, High valence state of Ni and Mo synergism in NiS₂-MoS₂ hetero-nanorods catalyst with layered surface structure for urea electrocatalysis, *J. Energy Chem.*, 2022, **66**, 483-492.
- [7] H. Yang, M. Yuan, Z. Sun, D. Wang, L. Lin, H. Li, G. Sun, High valence state of Ni and Mo synergism in NiS₂-MoS₂ hetero-nanorods catalyst with layered surface structure for urea electrocatalysis, *ACS Sustainable Chem. Eng.*, 2020, **8**, 8348-8355.
- [8] G. Zhao, Y. Xing, Y. Liu, X. Wang, B. Zhang, L. Mu, W. Liao, X. Xu, Built-in electric field in bifunctional electrocatalyst (Ni₃S₂@ Ni₉S₈) for high-efficiency OER and overall water splitting performance, *Mater. Today Chem.*, 2023, **34**, 101758.
- [9] L. Chai, Z. Hu, X. Wang, Y. Xu, L. Zhang, T. T. Li, Y. Hu, J. Qian, S. Huang, Stringing Bimetallic Metal-Organic Framework-Derived Cobalt Phosphide

- Composite for High-Efficiency Overall Water Splitting, *Adv. Sci.*, 2020, **7**, 1903195.
- [10]H. Song, S. Guo, X. Zhang, Y. Yang, B. Gao, Y. Pi, C. Pi, P. K. Chu, K. Huo, In-Situ and controllable construction of Mo₂N embedded Mo₂C nanobelts as robust electrocatalyst for superior pH-universal hydrogen evolution reaction, *J. Alloys Compd.*, 2022, **918**, 165611.
- [11]X. Zhang, Y. Liang, Nickel hydr(oxy)oxide nanoparticles on metallic MoS₂ nanosheets: a synergistic electrocatalyst for hydrogen evolution reaction, *Adv. Sci.*, 2018, **5**, 1700644.
- [12]K. Lan, L. Gong, M. Yang, X. Huang, P. Jiang, K. Wang, L. Ma, R. Li, Nitrogen and phosphorus dual-doping carbon shells encapsulating ultrafine Mo₂C particles as electrocatalyst for hydrogen evolution, *J. Colloid Interface Sci.*, 2019, **553**, 148-155.
- [13]S. Bolar, S. Shit, J. S. Kumar, N. C. Murmu, R. S. Ganesh, H. Inokawa, T. Kuila, Optimization of active surface area of flower like MoS₂ using V-doping towards enhanced hydrogen evolution reaction in acidic and basic medium, *Appl. Catal. B: Environ.*, 2019, **254**, 432-442.
- [14]L. Huang, G. Wei, J. Wang, D. Li, S. Jia, S. Wu, T. Jiang, Y. Guo, Y. Liu, F. Ren, Ion Irradiation Activated Catalytic Activity of MoSe₂ Nanosheet for High-Efficiency Hydrogen Evolution Reaction, *Adv. Energy Mater.*, 2023, **13**, 2300651.
- [15]X. Jia, H. J. Kang, X. X. Yang, Y. L. Li, K. Cui, X. H. Wu, W. Qin, G. Wu, Amorphous Ni(III)-based sulfides as bifunctional water and urea oxidation anode electrocatalysts for hydrogen generation from urea-containing water, *Appl. Catal. B: Environ.*, 2022, **312**, 121389.
- [16]J. Y. Zhang, T. He, M. D. Wang, R. J. Qi, Y. Yan, Z. H. Dong, H. F. Liu, H. M. Wang, B. Y. Xia, Energy-saving hydrogen production coupling urea oxidation over a bifunctional nickel-molybdenum nanotube array, *Nano Energy*, 2019, **60**, 894-902.
- [17]N. Chen, Y. X. Du, G. Zhang, W. T. Lu, F. F. Cao, Amorphous nickel

sulfoselenide for efficient electrochemical urea-assisted hydrogen production in alkaline media, *Nano Energy*, 2021, **81**, 105605.